34. Prestrelski SJ, Pikal KA, Arakawa T. 1995. Optimization of lyophilization conditions for recombinant human interleukin-2 by dried-state conformational analysis using Fourier-transform infrared spectroscopy. Pharm Res 12:1250–1259.
35. Carpenter JF, Prestrelski SJ, Dong A. 1998. Application of infrared spectroscopy to development of stable lyophilized protein formulations. Eur J Pharm Biopharm 45:231–238.
36. Cicerone MT, Soles CL. 2004. Fast dynamics and stabilization of proteins: Binary glasses of trehalose and glycerol. Biophys J 86:3836–3845.
37. Cicerone MT, Soles CL, Chowdhuri Z, Pikal MJ, Chang L. 2005. Fast dynamics as a diagnostic for excipients in preservation of dried proteins. Am Pharm Rev 8:22, 24–27.
38. Roe RJ. 2000. Methods of X-Ray and neutron scattering in polymer science. New York: Oxford University Press. p. 352.
39. Wang B, Tchessalov S, Cicerone MT, Warne N, Pikal MJ. 2009. Impact of sucrose level on storage stability of proteins in freeze-dried solids: II. Correlation of aggregation rate with protein structure and molecular mobility. J Pharm Sci 98:3145–3166.
40. Yoshioka S, Miyazaki T, Aso Y, Kawanishi T. 2007. Significance of local mobility in aggregation of beta-galactosidase lyophilized with trehalose, sucrose or stachyose. Pharm Res 24:1660–1667.
41. Luthra SA, Utz M, Pikal MJ. 2008. Solid state 13C NMR investigation of impact of annealing in lyophilized glasses. J Pharm Sci 97:4336–4346.
42. Webb SD, Cleland JL, Carpenter JF, Randolph TW. 2003. Effects of annealing lyophilized and spray-lyophilized formulations of recombinant human interferon-r. J Pharm Sci 92:715–729.
43. Surana R, Pyne A, Suryanarayanan R. 2004. Effect of aging on the physical properties of amorphous trehalose. Pharm Res 21:867–874.
44. Earle JP, Bennett PS, Larson KA, Shaw R. 1991. The effects of stopper drying on moisture levels of Haemophilus influenzae conjugate vaccine. Dev Biol Stand 74:203–210.
45. Donovan PD, Corvari V, Burton MD, Rajagopalan N. 2007. Effect of stopper processing conditions on moisture content and ramifications for lyophilized products: Comparison of "low" and "high" moisture uptake stoppers. PDA J Pharm Sci Technol 61:51–58.
46. Pikal MJ, Shah S. 1992. Moisture transfer from stopper to product and resulting stability implications. Dev Biol Stand 74:165–179.
47. Chang L, Shepherd D, Sun J, Tang X, Pikal MJ. 2005. Effect of sorbitol and residual moisture on the stability of lyophilized antibodies: Implications for the mechanism of protein stabilization in the solid state. J Pharm Sci 94:1445–1455.
48. Luthra SA, Hodge IM, Pikal MJ. 2008. Effects of annealing on enthalpy relaxation in lyophilized disaccharide formulations: Mathematical modeling of DSC curves. J Pharm Sci 97:3084–3099.
49. Shultz A, Young A. 1980. DSC on freeze-dried poly(methyl methacrylate)-polystyrene blends. Macromolecules 13:663–668.
50. Pikal MJ, Rigsbee DR, Roy ML. 2007. Solid state chemistry of proteins: I. Glass transition behavior in freeze dried disaccharide formulations of human growth hormone (hGH). J Pharm Sci 96:2765–2776.
51. Sartor G, Johari G. 1994. Calorimetric studies of the kinetic unfreezing of molecular motions in hydrated lysozyme, hemoglobin, and myoglobin. Biophys J 66:249–258.
52. Borde B, Bizot H, Vigier G, Buleon A. 2002. Calorimetric analysis of the structural relaxation in partially hydrated amorphous polysaccharides. II. Phenomenological study of physical ageing. Carbohydr Polym 48:111–123.
53. Vyazovkin S, Dranca I. 2006. Probing beta relaxation in pharmaceutically relevant glasses by using DSC. Pharm Res 23:422–428.
54. Gunawan L, Johari G, Shanker R. 2006. Structural relaxation of acetaminophen glass. Pharm Res 23: 967–979.
55. Pikal MJ, Rigsbee D, Roy MJ. 2008. Solid state stability of proteins III: Calorimetric (DSC) and spectroscopic (FTIR) characterization of thermal denaturation in freeze dried human growth hormone (hGH). J Pharm Sci 97:5122–5131.
56. Lunkenheimer P, Wehn R, Schneider U, Loidl A. 2005. Glassy aging dynamics. Phys Rev Lett 95:1–4.
57. Nagai K, Freeman BD, Watanabe T, Nakagawa T. 1999. Effects of physical aging on gas permeability and molecular motion in poly(1-trimethylsilyl-1-propyne), ACS Symposium Series, Vol. 733, pp. 95–101.
58. Smits ALM, Ruhnau FC, Vliegenthart JFG, Van Soest JJG. 1998. Aging of starch based systems as observed with FT-IR and solid state NMR spectroscopy. Starch/Staerke 50:478–483.
59. Etienne S, Hazeg N, Duval E, Mermet A, Wypych A, David L. 2007. Physical aging and molecular mobility of amorphous polymers. J Non-Cryst Solids 353:3871–3878.
60. Perez J, Cavaille JY, David L. 1999. New experimental features and revisiting the alpha and beta mechanical relaxation in glasses and glass-forming liquids. J Mol Struct 479:183–194.
61. Perez J, Cavaille JY, Diaz Calleja R, Gomez Ribelles JL, Monleon Pradas M, Ribes Greus A. 1991. Physical aging of amorphous polymers. Theoretical analysis and experiments on poly(methyl methacrylate). Makromol Chem 192:2141–2161.
62. Muzeau E, Vigier G, Vassoille R. 1994. Physical aging phenomena in an amorphous polymer at temperatures far below the glass transition. J Non-Cryst Solids 172–174:575–579.

63. Muzeau E, Vigier G, Vassoille R, Perez J. 1995. Changes of thermodynamic and dynamic-mechanical properties of poly(methyl methacrylate) due to structural relaxation-low-temperature aging and modeling. Polymer 36:611–620.
64. Hill JJ, Shalaev EY, Zografi G. 2005. Thermodynamic and dynamic factors involved in the stability of native protein structure in amorphous solids in relation to levels of hydration. J Pharm Sci 94: 1636–1667.
65. Bhugra C, Shmeis R, Krill SL, Pikal MJ. 2006. Predictions of onset of crystallization from experimental relaxation times. I—Correlation of molecular mobility from temperatures above the glass transition to temperatures below the glass transition. Pharm Res 23:2277–2290.

DOI 10.1002/jps

Journal of Controlled Release 148 (2010) 160–167

Contents lists available at ScienceDirect

Journal of Controlled Release

journal homepage: www.elsevier.com/locate/jconrel

Polyion complex micelle MRI contrast agents from poly(ethylene glycol)-*b*-poly(L-lysine) block copolymers having Gd-DOTA; preparations and their control of T_1-relaxivities and blood circulation characteristics

Kouichi Shiraishi [a], Kumi Kawano [b], Yoshie Maitani [b], Masayuki Yokoyama [c,*]

[a] Kanagawa Academy of Science and Technology, Yokoyama "Nano-medical Polymer" Project, KSP East 404, Sakado 3-2-1, Takatsu-ku, Kawasaki, Kanagawa 213-0012, Japan
[b] Institute of Medicinal Chemistry, Hoshi University, 2-4-41 Ebara, Shinagawa-ku, Tokyo 142-8501, Japan
[c] Medical Engineering Laboratory, Research Center for Medical Science, Jikei University School of Medicine, Nishi-shinbashi 3-25-8, Minato-ku, Tokyo 105-8461, Japan

ARTICLE INFO

Article history:
Received 9 June 2010
Accepted 12 August 2010
Available online 6 September 2010

Keywords:
Polymeric micelle
MRI contrast agent
Polyion complex
T_1-relaxivity (r_1)

ABSTRACT

The current study synthesized macromolecular magnetic resonance imaging (MRI) contrast agents constituted of the poly(ethylene glycol)-b-poly(L-lysine) block copolymer (PEG-P(Lys)). A chelate group, 1,4,7,10-tetraazacyclododecane-1,4,7,10-tetraacetic acid (DOTA), was attached to the primary amino group of the block copolymer in desired contents. Gd-DOTA-based macromolecular contrast agents were prepared from PEG-P(Lys) having DOTA (PEG-P(Lys-DOTA) and Gd(III) ions. All of the PEG-P(Lys) block copolymers having gadolinium ions (PEG-P(Lys-DOTA-Gd)) showed higher T_1 relaxivity (per gadolinium), $r_1 = 5.6$–$7.3\ mM^{-1}s^{-1}$, than that of a low-molecular-weight gadolinium-chelate, diethylenetriaminepentaacetic acid-gadolinium(III) (Gd-DTPA) at 9.4 T. The study prepared the polyion complex (PIC) micelles from the amino groups of the lysine units and an oppositely charged polyanion, poly(methacrylic acid) or dextran sulfate, in an aqueous medium. In contrast, the fully DOTA-attached PEG-P(Lys-DOTA-Gd) formed a PIC with a polycation. Compared with partially DOTA-attached cationic PEG-P(Lys-DOTA-Gd), this PIC micelle yielded a forty percent decrease of r_1. This r_1 decrease was considered to result from a change in the accessibility of water molecules to gadolinium ions in the micelles' inner core. The r_1 was decreased upon formation of the PIC micelle, and this change proved that our concept worked *in vitro*. Blood-circulation characteristics of PIC micelles were controlled by means of changing the molecular weight of the counter anion. The PIC micelles accumulated in tumor tissues, and MRI study showed T1W image of axial slice of tumor area was significantly enhanced at 24 h after the injection.

1. Introduction

In clinical use, magnetic resonance imaging (MRI) contrast agents have great potential to help distinguish between normal tissues and abnormal ones. Low-molecular-weight gadolinium chelates [1,2] are well-known as a positive contrast agent that provides a tell-tale white image. The essential function of the positive contrast agent is to shorten the T_1 relaxation time of water's protons. Low-molecular-weight contrast agents such as Gd-DTPA (diethylenetriaminepentaacetic acid gadolinium), however, have exhibited several disadvantages such as relatively low T_1 relaxivity (r_1), non-specific distribution to the whole body except in case of brain tumors. In terms of r_1 ($mM^{-1}s^{-1}$), it is well-known that fast rotation of low-molecular-weight chelates limits their relaxivities at a low level. In contrast, macromolecular gadolinium chelates have been actively studied. These include PEG [3], poly(L-lysine) [4,5], poly(glutamic acid) [6,7], dendrimer [8–10], and dextran [11,12]. As well as these macromolecular contrast agents, supramolecular systems [13–24] including liposomes [13,14], micelles [15,16], and other such systems [17–26] for MRI contrast agents have been the subjects of active research. The large sizes of these macromolecular systems result in a higher r_1 owing to slow tumbling of the macromolecules. In comparison with low-molecular-weight gadolinium–chelate contrast agents, advantages of these macromolecular systems are high r_1 and long residential periods in the bloodstream. Owing to these advantages, researchers have studied firstly macromolecular contrast agents as so-called "blood-pool agents" that provide high contrast in the blood vessels for a long time period. In addition to this use, the macromolecular systems MRI contrast agents may have a function as tumor-specific contrast agents. In the field of drug targeting, these nano-sized carrier systems inherently possess the ability to target solid tumors owing to a passive targeting mechanism, the enhanced permeability and retention (EPR) effect [27–29].

Bogdanov et al. reported highly specific tumor delivery of their contrast agent by the passive targeting mechanism [5]. In this study, the contrast-agent concentration in the blood, however, was similar

* Corresponding author. Tel.: +81 3 3433 1111x2336; fax: +81 3 3459 6005.
E-mail address: masajun2093ryo@jikei.ac.jp (M. Yokoyama).

0168-3659/$ – see front matter © 2010 Elsevier B.V. All rights reserved.
doi:10.1016/j.jconrel.2010.08.018

to that at the tumor sites even five days after intravenous injection. This result indicates problems underlying the use of macromolecular agents as such a diagnostic agent; too high a molecular weight of a contrast agent can result in a failure to excrete the agents from the body, and a high concentration of contrast agents in the blood can result in undesirable background images of normal tissues.

Our previous results regarding a polymeric micelle MRI contrast agent showed a successful delivery of the contrast agent to the target solid-tumor tissues [33]. This stably formed polymeric micelle MRI contrast agent exhibited a long circulation in blood resulting in a significant amount of delivery to target solid-tumor tissues in colon 26 bearing mice. The T_1-weighted signal intensity of the MR image at 24 h after the injection was greatly increased. Even though we achieved this successful targeting of the contrast agent, the obtained coronal slice image exhibited its highest signal in the heart and aorta area, because greater than 20% of the injected dose was remained in blood.

In spite of these attractive potentials of the macromolecular contrast agents, no macromolecular MRI contrast agent has presently obtained approval in these types for clinical use mainly owing to its toxicity [1]. In contrast to the anti-cancer drug targeting based on the EPR effect, in which a lengthy circulation in the bloodstream is a prerequisite for the targeting, slow excretion of the macromolecular contrast agents from the body can be a problem related to toxicity. This problem can be solved if the dose of the macromolecular agents is much lower than that of low-molecular-weight contrast agents, and if the efficient tumor targeting is achieved.

Our previous report proposed MRI contrast agents based on the charged block copolymer as shown in Fig. 1 [30]. In addition to the tumor-targeting ability of polymeric micelles, changeable r_1 of the contrast agent depending on the formation and the dissociation of the micelle structures may have a great potential to solve the aforementioned problem that commonly characterizes macromolecular contrast agents. During polymeric micelles' long circulation period in the blood stream, r_1 is suppressed at a low level. The formation inhibits water molecules' access to gadolinium ions in the inner core of polymeric micelle. At the solid-tumor sites, the polymeric micelles are expected to be gradually dissociated into single polymer chains. The accumulated single polymer chains exhibit high r_1, because water molecules easily access the gadolinium ions. Also, single block copolymers have a molecular weight less than 30,000 that can be excreted from the kidneys. To carry out this strategy for tumor-selective MRI contrast agents, this report presents the preparation of stably chelated block copolymer MRI contrast agents having high r_1 and polyion complex (PIC) micelles having low r_1 that can suppress the background MR signal regarding, for example, blood vessels. These points may greatly facilitate efforts to decrease doses and, in turn, to minimize toxicity. Since the low binding constant of gadolinium chelates related heavily to nephrogenic systemic fibrosis, (NSF) [31], coordination of gadolinium ions must take place without unfavored chelation. Macrocyclic 1,4,7,10-tetraazacyclododecane-1,4,7,10-tetraacetic acid (DOTA) forms a more thermodynamically stable and kinetically inert complex than DTPA [32]. A new combination of poly (ethylene glycol)-b-poly(L-lysine) (PEG-P(Lys)) and DOTA was selected for our chemistry. This combination gives us a more facile synthesis and a more stable metal chelation [1].

Herein, this paper presents preparation of a PEG-P(Lys) block copolymers-based MRI contrast agent as well as characterization of its paramagnetic property (r_1) of both the block copolymer and the PIC micelles. Control of the blood circulation property and the biodistribution of our PIC micelle MRI contrast agents is reported.

2. Materials and methods

2.1. Materials

A chelating agent active ester, 1,4,7,10-tetraazacyclododecane-1,4,7,10-tetraacetic acid mono (N-hydroxysuccinimide ester) (DOTA-OSu), was purchased from Macrocyclics, Texas, USA. Poly(methacrylic acid sodium salt) ($M_w = 7750$) was purchased from Fluka, Tokyo, Japan. Dextran sulfate sodium salt from Leuconostoc spp. (average of $M_w = \sim 8000$ and >500,000), diethylenetriaminepentaacetic acid gadolinium dihydrogen salt hydrated (Gd-DTPA), and deuterium solvents were purchased from Sigma-Aldrich, Tokyo, Japan. Gadolinium chloride hexahydrate ($GdCl_3 \cdot 6H_2O$) was purchased from Wako Pure Chemicals Industries, Ltd., Tokyo, Japan. Polyallylamine (average $M_w = 5000$, 15,000, 60,000) was a kind gift from Nitto Boseki Co., Ltd., Tokyo, Japan. All these commercial reagents were used as purchased. A dialysis membrane Spectrapor 6 (molecular weight cut off (MWCO) = 1000) was purchased from Spectrum Laboratories Inc., Tokyo, Japan. Different lengths of α-methoxy-ω-aminopropyl-poly (ethylene glycol) (PEG-NH_2, Mw = 5200 and 12,000) were purchased from NOF Corporation, Tokyo, Japan, and benzene-based lyophilization was carried out before use.

^{1}H-NMR spectra were recorded on a Varian UNITY INOVA 400 MHz NMR spectrometer. For measurements of the gadolinium ion contents in block copolymer conjugates, inductively coupled plasma (ICP) with an SPS7800 apparatus (SII NanoTechnology Inc., Tokyo, Japan) was used. Measurements of T_1 relaxation time were carried out with a Varian UNITY INOVA 400 MHz NMR spectrometer, and the measurements featured an inversion recovery pulse sequence. In vitro MR images were obtained on a Varian 400 NMR system equipped with a 9.4 T magnet and an imaging probe. The T_1-weighted gradient echo phantom images of 0.25 mM of Gd-DTPA, the block copolymers, and their PIC micelles were acquired with the following parameters: TR/TE = 7.3/3.9 for the 118-23-23-7 system (FOV = 3.7 × 2.2 cm^2), 5.2/2.4 for the 118-65-13-10 system (FOV = 3.0 × 4.3 cm^2), and a flip angle of 30°. Dynamic light scattering (DLS) measurements were carried out at 24.5 °C with a DLS-700 instrument (Otsuka Electronics Co., Ltd., Tokyo Japan).

2.2. Animals

Five-week-old ddY female mice and CDF_1 female mice were purchased from the Sankyo Labo Service Corporation, Tokyo, Japan. All animal experiments were carried out in accordance with the

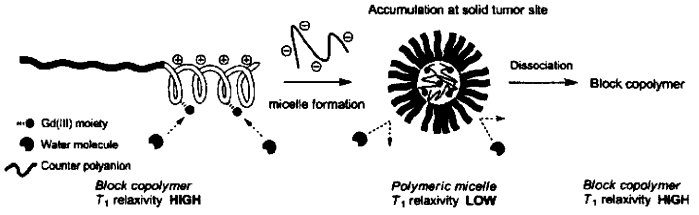

Fig. 1. Conception of tumor-specific PIC micelle MRI contrast agent.

guidelines of the Guiding Principles for the Care and Use of Laboratory Animals of Hoshi University.

2.3. Synthesis of PEG-P(Lys-DOTA-Gd)

Poly(ethylene glycol)-b-poly(L-lysine-DOTA) (PEG-P(Lys-DOTA)) was synthesized according to the literature [33]. The obtained PEG-P(Lys-DOTA), which had 118 ethylene glycol units and 65 lysine units and 13 DOTA moieties, was coded as 118-65-13. All the PEG-P(Lys-DOTA) with different PEG lengths, lysine units, and DOTA numbers were synthesized according to the same method. The composition of PEG-P(Lys-DOTA) was determined by means of ^{1}H-NMR in D_2O under an alkali condition (pH>10). ^{1}H-NMR spectra of all the block copolymers are available in supplemental data (S1).

$GdCl_3 \cdot 6H_2O$ (41.0 mg, 0.110 mmol, 15 mole equivalents to the block copolymer) was added to PEG-P(Lys-DOTA) (118-65-13, 135.1 mg) in H_2O (11.0 mL), and the solution was maintained at a pH range of 6.0–6.5 by an addition of aqueous NaOH. The reaction mixture was stirred for 3 h at 50 °C, followed by dialysis, at first, against 0.02 N HCl and, then, against dist. H_2O 5 times. PEG-P(Lys-DOTA-Gd) was obtained as a white solid after lyophilization (137.5 mg). The content of the gadolinium ions was measured by means of ICP analysis (7.7 wt.%, the number of gadolinium ions per polymer chain was 10). The obtained PEG-P(Lys-DOTA-Gd) was coded as 118-65-13-10.

2.4. Preparation of PIC micelles

PEG-P(Lys-DOTA-Gd) (118-65-13-10) and poly(methacrylic acid) (M_w = 7750) were mixed in various mixing ratios at pH 7.3–7.4. On the other hand, PEG-P(Lys-DOTA-Gd) (118-23-23-7) was mixed with poly(allylamine) (M_w = 15,000) in the equivalent charge ratio (CO_2H of the empty DOTA moiety/NH_2 of poly(allylamine) = 1/1) at pH 7.3–7.4. The size of the above-mentioned two types of obtained PIC micelle solutions was determined by means of DLS in either a phosphate buffer solution (10 mM PBS, pH = 7.3) or 150 mM NaCl at 24.5 °C [33], and their T_1 relaxation times were measured according to the aforementioned steps. DLS charts of these PIC micelles are available in supplemental data (S2).

2.5. Measurement of T_1 relaxation time

The longitudinal relaxation times (T_1) of the PEG-P(Lys-DOTA-Gd) solutions and of the PIC micelle solutions were measured by means of the standard-inversion recovery method in four different concentrations below 2.0 mM of the gadolinium ion concentration at 22–24 °C. Longiditunal relaxivity (r_1) was calculated according to the following equation:

$$(1/T_1)_{obs} = (1/T_1)_d + r_1 \cdot [Gd],$$

where [Gd] is a concentration of the gadolinium ion, $(1/T_1)_{obs}$ is an observed relaxation rate, and $(1/T_1)_d$ is the relaxation rate of water protons.

2.6. PIC micelles using 2 different molecular weights of dextran sulfate

Each amount of the molecular weight of the dextran sulfate (M_w = 500 kDa, dex500k) in H_2O was dropwised in a tiny portion of a PEG-P(Lys-DOTA-Gd) solution (4 mg/mL), and stirred for 10 min at room temperature. Then, dextran sulfate (M_w = 8 kDa, dex8k) was added to the mixture to control the cation/anion ratio (SO_3H/NH_2 = 1.2), and was stirred at room temperature over night. The obtained diluted PIC micelles were concentrated by means of a nitrogen flow at 40 °C until the concentration became 15 mg/mL. The solutions were filtered through 1.0 μm of a nylon membrane for *in vitro* study and through 0.22 μm of a PES membrane for *in vivo* study.

2.7. Measurements of gadolinium (III) concentration in blood

PIC micelles were prepared by mixing PEG-P(Lys-DOTA-Gd) and dextran sulfate as described in the above section. Five-week-old female ddY mice (body weight = 20–22 g) were intravenously injected from the tail vein at a dose of 0.05 mmol Gd/kg of body weight. According to a defined schedule, a blood sample (ca. 10–80 μL) was taken from a tail vein through a glass capillary. Saline (1.5 mL) was added to this blood sample, followed by centrifugation (13,000 rpm, 4 °C). The supernatant was applied to inductively coupled plasma (ICP) measurements for Gd content determination. The Gd content in the plasma was calculated as a percentage % of the injected dose with an estimation of plasma volume being 4.9 v/w % of body weight [35].

2.8. Biodistribution of PIC micelles and MRI study in colon 26 bearing mice

Biodistribution and MR imaging was performed with female mice (CDF_1) bearing a colon 26 tumor. The contrast agents were injected at a dose of 0.05 mmol of Gd/kg into a mice-tail vein. MR images were taken with a Varian NMR system at 9.4 T. T2-weighted fast spin echo (TR = 2500 ms, ETL = 8, ESP = 4, effective TE = 48) (T2W-SE) was performed for all experiments before following the T1-weighted gradient echo protocol (T1W-GE). Parameters of the T1W-GE were TR/TE = 8.0/4.5, flip angle = 30°, field of view of 45 × 45 mm, a matrix size of 192 × 192, and thickness of 2 mm. For normalized signal intensity relative to the T1-weighted images, the tumor area was selected as a region of interest (ROI). The signal intensity of the ROI was compared with the intensity of a stock solution of 0.1 mM gadolinium ion in agarose gel. The major tissues including tumor tissues were excised. The determination of gadolinium ion content in the tissue was measured by means of ICP [33].

3. Results

3.1. Synthesis of gadolinium contained block copolymer and their r_1

Poly(ethylene glycol)-b-poly(L-lysine) (PEG-P(Lys)) block copolymers were synthesized by means of the polymerization of ε-(Benzyloxycarbonyl)-L-lysine *N*-carboxyanhydride (Lys(Z)-NCA) from PEG-NH_2 [33,34]. By control of the DOTA-OSu/polymer ratio, PEG-P(Lys-DOTA) having the desired DOTA moiety numbers was successfully prepared. The control of the gadolinium ion number was simpler and more accurate than the previous results without any unfavored coordination [31]. The code of block copolymers indicates each set of units pertaining to the segments. For example, 118-65-13 indicates 118 units of PEG (molecular weight = 5,200), 65 units of lysine, and 13 units of DOTA moiety. Table 1 summarizes the obtained compositions of PEG-P(Lys-DOTA-Gd).

All of the obtained block copolymers that were conjugated with gadolinium ions exhibited larger r_1 values than did the Gd-DTPA (r_1 = 3.7), as shown in Table 1. The r_1 values of the block copolymers having a PEG molecular weight of 5,200 were nearly the same values (5.6–6.2), even at different P(Lys) lengths and for different numbers of DOTA units (runs 1–3 in Table 1). In contrast, the r_1 of run 4, which had the longer PEG chain (molecular weight = 12,000) (run 4 in Table 1), exhibited a larger r_1 value than did the r_1 of run 1, which had a similar P(Lys) chain length, a similar DOTA unit number, and a similar gadolinium number. This finding indicates that, to a certain extent, PEG blocks' chain length affect the r_1. This result showed opposite r_1 behavior to compare with our previous PEG-P(Asp) system [30], which obtained higher r_1 value in shorted PEG chain. This

Table 1
Composition and r_1 of PEG-P(Lys-DOTA-Gd).

Run	Polymer code	Unit number M_w		DOTA/unit	Gd/number	M_w/(x10^3)	r_1[a]/mM^{-1} s^{-1}
		PEG	P(Lys)				
1	118-23-9-7	118/5200	23/2900	9	7	12.7	5.6
2	118-23-23-7	118/5200	23/2900	23	7	18.1	6.2
3	118-65-13-10	118/5200	65/8300	13	10	20.1	6.1
4	272-22-10-8	272/12000	222800	10	8	19.9	7.3

[a] r_1 value was measured at 9.4 T. r_1 value of Gd-DTPA at 9.4 T was 3.7

r_1 behavior might be affected the substitution at the side chain and hydrophobicity of the blocks.

3.2. Preparation of PIC micelles and DLS measurement

In the present study, the preparation of PIC micelles involved mixing PEG-P(Lys-DOTA-Gd) and a counter polyion, either cationic or anionic. Dynamic light scattering (DLS) was used for determination of the size of PIC micelles. PEG-P(Lys-DOTA-Gd) having a longer P(Lys) chain (118-65-13-10, run 3 in Table 1) with poly(methacrylic acid) (M_w = 7750) formed a PIC micelle whose weight-weighted average diameter was 30 nm accompanied with a small fraction of the secondary aggregation (the average, 169 nm) as shown in Fig. 2(a) (type 1). By mixing 118-65-13-10 with dextran sulfate (M_w = 8000) instead of poly(methacrylic acid), we obtained a similar weight-weighted distribution average of 33 nm and a secondary aggregation average of 173 nm. A longer P(Lys) chain of PEG-P(Lys-DOTA-Gd) (118-65-13-10) induced a formation of PIC micelle. Further studies of PIC micelles' are described in the supplemental data (S3).

Micelle-forming behaviors of PEG-P(Lys-DOTA-Gd), 118-23-23-7, were measured in the amino groups of the lysine units that were fully substituted with the DOTA moiety (23 units), and gadolinium ions were partially coordinated in DOTA (7 out of 23 units). Namely, 118-23-23-7 had 16 uncoordinated (vacant) DOTA units. The uncoordinated DOTA moiety had 4 tertiary amine groups and 3 carboxylic acid groups as donating groups. Totally negative charge of DOTA groups can interact with oppositely charged polymer, such as poly(allylamine)s. The successful preparation of PIC micelles involved mixing 118-23-23-7 with cationic poly(allylamine) as shown in Fig. 2(b) (type 2). Indeed, this micelle formation occurred even though 118-23-23-7 had only the short P(Lys) chain length. The size of a given PIC micelle depended on the molecular weight of poly(allylamine) (data available in supplemental data S2).

3.3. MRI phantom study of the PIC micelles

As shown in run 1 of Table 2, the r_1 of the PIC micelles was lower than the r_1 of the block copolymer itself when we mixed 118-65-13-10 with poly(methacrylic acid). For r_1, PIC micelles forming from 118-23-23-7 and poly(allylamine) (M_w = 15,000) exhibited a considerable decrease in the r_1. The r_1 value of the PIC micelles dropped to 3.8 whereas that of the parent block copolymers was 6.2, as summarized in run 2 of Table 2. Even though this r_1 difference between the block copolymers and the PIC micelles was not as large as the previously reported system (PEG-P(Asp-DTPA-Gd) with poly(allylamine)) [30], the PEG-P(Lys)-based system exhibited a significant r_1 difference.

Fig. 3 shows T_1-weighted MR images of a phantom at 9.4 T. All of the MRI phantom images were recorded at 0.25 mM of gadolinium ions in 0.15 M of aqueous NaCl solution. Both the PEG-P(Lys-DOTA-Gd) of 118-65-13-10 and that of 118-23-23-7 showed images considerably more intense than the images shown by a low-molecular-weight Gd chelate Gd-DTPA. This is consistent with the r_1

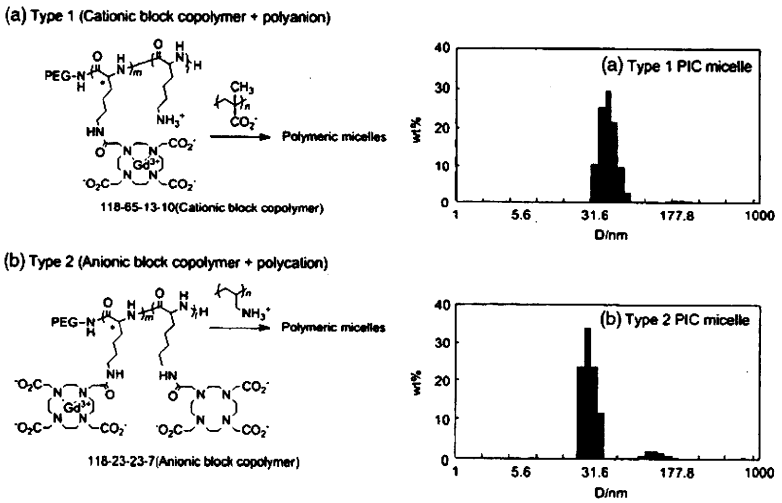

Fig. 2. Scheme of PIC micelle formation for both type 1 and type 2, and DLS charts of the PIC micelles. (a) 118-65-13-10 + poly(methacrylic acid) (Mw = 7,750), and (b) 118-23-23-7 + poly(allylamine) (Mw = 15,000). Ratio of CO_2H/NH_2 = 1/1.

Table 2
Change of r_1 values upon PIC micelle formation.

Run	Block copolymer	r_1[a]/mM^{-1} s^{-1}	Counter polymer[b]	Charge ratio (NH_2/CO_2H)	r_1[c]/mM^{-1} s^{-1}
1	118-65-13-10	6.1	Anion/Poly(methacrylic acid)	1/2	5.2
2	118-23-23-7	6.2	Cation/Poly(allylamine)	2/1	3.8

[a] Without micelle formation at 9.4 T.
[b] Poly(methacrylic acid) (M_w = 7,750), poly(allylamine) (M_w = 15,000).
[c] After micelle formation at 9.4 T.

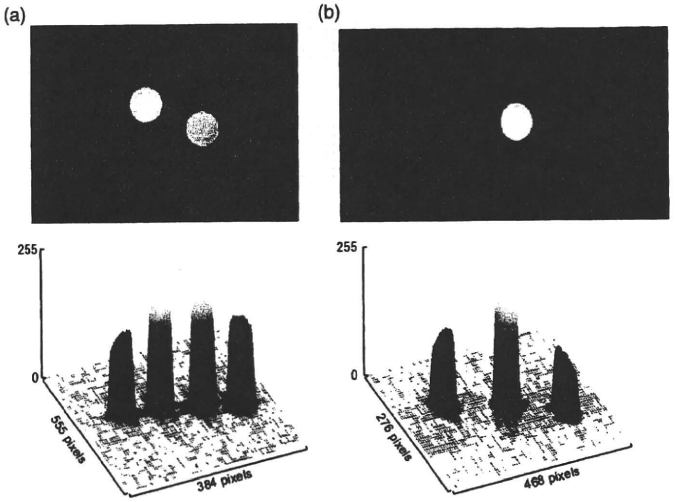

Fig. 3. MRI phantom images of 0.25 mM Gd solutions in 0.15 M NaCl at 9.4 T. (a) (left to right) Gd-DTPA, 118-65-13-10, PIC micelle with dextran sulfate, and poly(methacrylic acid). TR/TE = 7.3/3.9. (b) (left) Gd-DTPA, (center) 118-23-23-7, (right) PIC micelle with poly(allylamine). TR/TE = 5.2/2.4.

data in Table 1. In contrast, the PIC micelle solution yielded clearly darker images than did the parent block copolymers in the two cases of PEG-P(Lys-DOTA-Gd), 118-65-13-10 and 118-23-23-7. These results confirm that the formation of the PIC micelles lowered the signal intensity of the T_1-weighted image.

3.4. Measurements of gadolinium(III) concentration in blood

To obtain appropriate pharmacokinetics of the contrast agent, we prepared-as a polyanion-PIC micelles, themselves prepared from a larger molecular weight of dextran sulfate (M_w = 500 kDa, dex500k) and a lower molecular weight of dextran sulfate (M_w = 8 kDa, dex8k). The preparation of the PIC micelles involved mixing various ratios of dex500k and dex8k. The obtained PIC micelles exhibited diameter whose cumulative size was 80–110 nm, exhibited near zero or slight negative ζ-potentials, and exhibited 20–30% decreases in r_1 as shown in Table 3. Fig. 4 shows pharmacokinetics of the obtained PIC micelles and the molecular weight of the dextran-sulfate effect on the blood-circulation behavior of PIC micelles. Control of the pharmacokinetic property involved changing the molecular weight of dextran sulfate for PIC micelle. This shows that there was a better Gd(III) concentration over time than a low-molecular-weight Gd chelate, Gd-DTPA; however, this concentration was not as stable as in the case of anti-cancer drug targeting (25% dose at 24 h post injection) [29]. But the optimum circulation characteristic for contrast agents may be less stable than the anti-cancer drug cases, since more rapid excretion may be desirable for toxicity concerns regarding the contrast agents.

Table 3
Mw dependence of dextran sulfate effect on formation of PIC micelles.

Run	SO_3H/ NH_2		Size/nm	ζ-potential/mV	r_1[a]/mM^{-1} s^{-1}
	dex500k/eq (vs. NH_2)	dex8k/eq (vs. NH_2)			
1	0	1.2	77.8	−1.4	4.7
2	0.3	0.9	88.5	−1.0	4.4
3	0.5	0.7	109.1	0.3	4.6
4	1.2	0	120.7	−7.3	4.4

[a] r_1 was measured at 9.4 T.

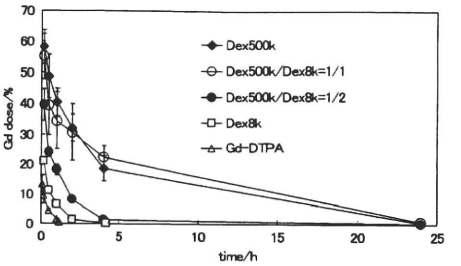

Fig. 4. Blood-concentration time course of PIC micelles of PEG-P(Lys-DOTA-Gd) with dextran sulfate at a dose of 0.05 mmol Gd/kg, and Gd-DTPA at a dose of 0.10 mmol Gd/kg in ddY female mice. Mean ± SD (n = 3).

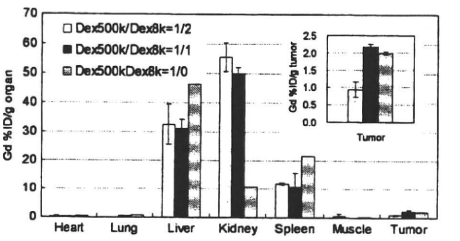

Fig. 5. Biodistribution of PEG-P(Lys-DOTA-Gd) with dextran sulfate micelle 24 h after the injection at a dose of 0.05 mmol Gd/kg.

3.5. Biodistribution of the PIC micelles and MRI study

We performed *in vivo* study of the PIC micelles which gave longer blood circulation (dex500k/dex8k = 1/2, 1/1, and dex500k only) in CDF_1 female mice bearing colon 26 tumor. Biodistribution of the PIC micelles depended on the ratio of dex500k and dex8k. When the mixing ratio of dex500k/dex8k was 1/2 or 1/1, we observed rapid clearance from the kidney. These results indicated that their PIC micelles were not stable in blood for long time. When we mixed PEG-P(Lys-DOTA-Gd) with dex500k only, higher accumulation in liver and spleen was obtained. In contrast, equal ratio of dex500k and dex8k showed better tumor accumulation and lower accumulation in liver and spleen (Fig. 5.)

In vivo MRI study of the obtained PIC micelle (dex500k/dex8k = 1/1) was performed. T_1-weighted gradient echo (T1W-GE) axial image was performed using Varian NMR system at 9.4 T. The signal intensities of tumor area were compared to before and after the injection of the contrast agent at a dose of 0.05 mmol Gd/kg. The signal intensity of the tumor area was slightly increased at post injection. This is caused by the contrast agent in blood. As shown in Fig. 6, significant enhancement (1.4 times) of T1W image in tumor area at 24 h after the injection was observed.

4. Discussions

We showed a facile synthesis of two types of PEG-P(Lys-DOTA); one possessed only DOTA-substituted lysine residues [33] and the other possessed both DOTA-substituted and unmodified lysine residues. This result demonstrates the easy and accurate molecular design of the PEG-P(Lys)-based MRI contrast-agent system. In the previous "PEG-P(Asp)-DTPA"-based system [30], unfavored gadolinium ions were coordinated to the aspartic acid residues. EDTA-2Na treatment removed gadolinium ions both the aspartic acid and the DTPA moieties. This was because lowered binding affinity of the DTPA-moiety by consuming one carboxylic acid for conjugation.

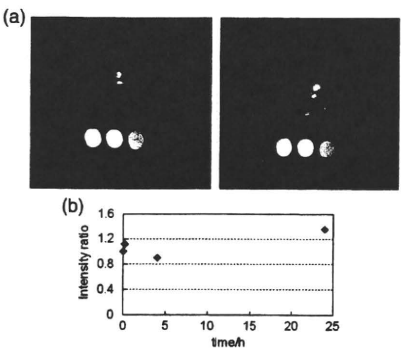

Fig. 6. (a) Axial MIP images of the axial slice (left) before and (right) 24 h after the injection at a dose of 0.05 mmol Gd/kg.(2 mm × 6 slices) (b) relative signal intensities of T1W-image of tumor area after the injection.

For the PEG-P(Lys)-based system, experimental conditions that eliminated unfavorable gadolinium ions, possibly coordinated to the lysine residues of PEG-P(Lys), were optimized. A significant level of gadolinium ions was observed to be coordinated with PEG-P(Lys) under the same reaction conditions as those characterizing the PEG-P(Lys-DOTA-Gd) synthesis (supplemental data S4). When the lysine residues along the polymer's main chain were condensed, they can bind gadolinium ions easily and stably. The EDTA-2Na treatment did not remove the gadolinium ions completely. However, a treatment of dialysis in 0.02 N HCl successfully removed the bound gadolinium ions. This condition was used for gadolinium chelation to PEG-P(Lys-DOTA).

The number of gadolinium ion in the polymer was saturated under above dialysis condition, even further addition of gadolinium ion to the block copolymer (supplemental data S5). Recent research shows that the use of gadolinium contrast agents increases the risk of a release of dissociated gadolinium ions, an event that would lead to NSF. This possibility has recently prompted the U.S. Food and Drug Administration to issue a public health advisory regarding gadolinium-containing contrast agents and a possible link to the development of NSF [31]. While it is necessary to employ a chelate with high thermodynamic stability, kinetic inertness is probably more important. In terms of the toxicity of the contrast agents, gadolinium ions must be stably chelated in high binding affinity.

Gadolinium-polymer conjugates can exhibit larger r_1 values than the parent low-molecular-weight Gd-chelates because, in aqueous media, the polymer-conjugates have limited rotative motion [36]. It should be noted that r_1 is dependent on magnetic-field strength [37], and this significant r_1 difference was observed at 9.4 T. We will perform, in future research, r_1 study to observe magnetic field dependence at 1.5 T as well as at 9.4 T. In this way, the obtained contrast between PIC micelles and block copolymers may greatly improve at clinically useful magnetic fields. Further experiments should yield more details about PIC formation and the magnetic-field effect on PIC micelles' r_1.

In the PEG-P(Lys) system, both the cation and the anion block copolymer decreased their r_1 when the PIC micelle formation took place. This fact greatly benefits our field for the following reasons. First, the toxicity of the PIC micelles is an important matter for in vivo studies. Clinical studies cannot use toxic contrast agents, even if they

have a great MRI contrast potential. The appropriate choice of non-toxic block copolymers and of counter ion polymers that offers a wide range of charges greatly helps minimize the toxicity of the PIC micelles. Second, a wide choice of various charged block copolymers and of counter ion polymers enables us to easily optimize the in vivo dissociation characteristic of the PIC micelles. An appropriate dissociation rate of the PIC micelle is essential to maximizing both the efficiency of solid-tumor targeting and the image contrast at the tumor site. A variety of choices is necessary for effective imaging and targeting. In addition, an appropriate design of PIC micelles will control the PIC micelles' inner-core environment and will, thereby, further decrease the PIC micelles' r_1; this decrease, in turn, will strengthen the contrast between solid-tumor sites and the bloodstream.

In vivo MRI study of our PIC micelles were performed in tumor bearing CDF_1 mice. The enhancement of T1W image in tumor area was observed at 24 h after the PIC micelle MRI contrast agents injection. This enhancement was not high as previously reported our polymeric micelle MRI contrast agent [33]. However, this MRI study and above *in vivo* biodistribution study indicated that stable blood circulation and selective and high accumulation in tumor gives great improvement of T1W image in tumor area at such dose of the contrast agent. We controlled the blood circulation property by means of the PIC preparation. This approach can be solved to obtain further stability in blood and high accumulation in tumor.

5. Conclusions

This study presented the preparation of stably gadolinium chelated block copolymer that formed polyion complex (PIC) micelle MRI contrast agents. The obtained block copolymer showed stable gadolinium chelation without unfavored coordination to the block copolymer. The PIC micelle MRI contrast agents lowered r_1, whereas their single block copolymers exhibited high r_1. This paper presented changes in r_1 between the cationic and anionic block copolymers and the PIC micelles *in vitro*. Significant decreases in r_1 were found when the PIC micelles formed in both cases. In particular, there was a 40% decrease in r_1 for the latter type 2 PIC micelle. The r_1-changeable PIC micelles MRI contrast agent is dependent on the formation and the dissociation of PIC micelles' structure. *In vitro*, our strategy worked well for a well-defined molecular system. Thus, our obtained results constitute a firm platform for future studies that aim to obtain a large contrast difference between block copolymers and micelles.

Pharmacokinetics and biodistribution of PIC micelles were controlled when a different molecular weight of dextran sulfate was used for the PIC micelle preparation. The PIC micelles worked not only to prolong the retention time in blood but also to diminish in vivo toxicity of a cationic block copolymer. The PIC micelles accumulated in tumor and MRI study showed significant enhancement by the injection of the contrast agent.

Acknowledgement

This work was supported by the Ministry of Health, Labour, and Welfare of Japan. K. Shiraishi and M. Yokoyama acknowledge the support from the Program for Promoting the Establishment of Strategic Research Centers, Special Coordination Funds for Promoting Science and Technology, the Ministry of Education, Culture, Sports, Science and Technology of Japan, and Tokyo Ohka Foundation for the Promotion of Science and Technology.

Appendix A. Supplementary data

Supplementary data to this article can be found online at doi:10.1016/j.jconrel.2010.08.018.

References

[1] P. Caravan, J.J. Ellison, T.J. McMurry, R.B. Lauffer, Gadolinium(III) chelates as MRI contrast agents: structure, dynamics, and applications, Chem. Rev. 99 (1999) 2293–2352.
[2] S. Aime, C. Cabella, S. Colombatto, S.G. Crich, E. Gianolio, F. Maggioni, Insights into the use of paramagnetic Gd(III) complexes in MR-molecular imaging investigations, J. Magn. Reson. Imaging 16 (2002) 394–406.
[3] D.M. Doble, M. Botta, J. Wang, S. Aime, A. Barge, K.N. Raymond, Optimization of the relaxivity of MRI contrast agents: effect of poly(ethylene glycol) chains on the water-exchange rates of Gd^{III} complexes, J. Am. Chem. Soc. 123 (2001) 10758–10759.
[4] V.S. Vexler, O. Clement, H. Schmitt-Willich, R.C. Brasch, Effect of varying the molecular weight of the MR contrast agent Gd-DTPA-polylysine on blood pharmacokinetics and enhancement patterns, J. Magn. Reson. Imaging 4 (1994) 381–388.
[5] A. Bogdanov Jr, S.C. Wright, E.M. Marecos, A.V. Bogdanova, C. Martin, R. Weissleder, A long-circulating co-polymer in "passive targeting" to solid tumors, J. Drug Target. 4 (5) (1997) 321–330.
[6] X. Wen, E.F. Jackson, R.E. Price, E.E. Kim, Q. Wu, S. Wallace, C. Charnsangavej, J.G. Gelovani, C. Li, Synthesis and characterization of poly(L-glutamic acid) gadolinium chelate: A new biodegradable MRI contrast agent, Bioconjugate Chem. 15 (2004) 1408–1415.
[7] F. Ye, T. Ke, E.-K. Jeong, X. Wang, Y. Sun, M. Johnson, Lu. Z-R, Noninvasive visualization of in vivo drug delivery of poly(L-glutamic acid) using contrast-enhanced MRI, Mol. Pharm. 3 (2006) 507–515.
[8] S. Langereis, Q.G. Lussanet, M.H.P. Genderen, W.H. Backes, E.W. Meijer, Multivalent contrast agents based on gadolinium-diethylenetriaminepentaacetic acid-terminated poly(propylene imine) dendrimers for magnetic resonance imaging, Macromolecules 37 (2004) 3084–3091.
[9] H. Kobayashi, S. Kawamoto, S.K. Jo, H.L. Bryant, M.W. Brechbiel, Macromolecular MRI contrast agents with small dendrimers: pharmacokinetic differences between sizes and cores, Bioconjugate Chem. 14 (2003) 388–394.
[10] J. Rudovsky', P. Hermann, M. Botta, S. Aime, I. Lukes, Dendrimeric Gd(III) complex of a monophosphinated DOTA analogue:optimizing relaxivity by reducing internal motion, Chem. Commun. (2005) 2390–2392.
[11] R. Rebizak, M. Schaefer, E. Dellacherie, Polymeric conjugates of Gd^{3+}-diethylene-triaminepentaacetic acid and dextran. 1. Synthesis, characterization, and paramagnetic properties, Bioconjugate Chem. 8 (1997) 605–610.
[12] M.M. Huber, A.B. Staubli, K. Kustedjo, K.K.M. Gray, J. Shih, S.E. Fraser, R.E. Jacobs, T.J. Meade, Fluorescently detectable magnetic resonance imaging agents, Bioconjugate Chem. 9 (1998) 242–249.
[13] W.J.M. Mulder, G.J. Strijkers, A.W. Griffioen, L.B. Bloois, G. Molema, G. Storm, G.A. Koning, K. Nicolay, A liposomal system for contrast-enhanced magnetic resonance imaging of molecular targets, Bioconjugate Chem. 15 (2004) 799–806.
[14] G.A.F. Tilborg, W.J.M. Mulder, P.T.K. Chin, G. Storm, C.P. Reutelingsperger, K. Nicolay, G.J. Strijkers, Annexin A5-conjugated quantum dots with a paramagnetic lipidic coating for the multimodal detection of apoptotic cells, Bioconjugate Chem. 17 (2006) 865–868.
[15] G. Zhang, R. Zhang, X. Wen, L. Li, C. Li, Micelles based on biodegradable poly(L-glutamic acid)-*b*-polylactide with paramagnetic Gd ions chelated to the shell layer as a potential nanoscale MRI-visible delivery system, Biomacromolecules 9 (2008) 36–42.
[16] H.Y. Lee, H.H. Jee, S.M. Seo, B.K. Kwak, G. Khang, S.H. Cho, Diethylenetriamine-pentaacetic acid-gadolinium (DTPA-Gd)-conjugated polysuccinimide derivatives as magnetic resonance imaging contrast agents, Bioconjugate Chem. 17 (2006) 700–706.
[17] D.D. Castelli, E. Gianolio, S.G. Crich, E. Terreno, S. Aime, Metal containing nanosized systems for MR-molecular imaging applications, Coord. Chem. Rev. 252 (2008) 2424–2443.
[18] M. Vaccaro, A. Accardo, D. Tesauro, G. Mangiapia, D. Lf, K. Schilln, O. Sderman, G. Morelli, L. Paduano, Supramolecular aggregates of amphiphilic gadolinium complexes as blood pool MRI/MRA contrast agents: Physicochemical characterization, Langmuir 22 (2006) 6635–6643.
[19] Z. Cheng, A. Tsourkas, Paramagnetic porous polymersomes, Langmuir 24 (2008) 8169–8173.
[20] S.R. Bull, M.O. Guler, R.E. Bras, T.J. Meade, S.I. Stupp, Self-assembled peptide amphiphile nanofibers conjugated to MRI contrast agents, Nano Lett. 5 (2005) 1–4.
[21] S.R. Bull, M.O. Guler, R.E. Bras, P.N. Venkatasubramanian, S.I. Stupp, T.J. Meade, Magnetic resonance imaging of self-assembled biomaterial scaffolds, Bioconjugate Chem. 16 (2005) 1343–1348.
[22] J. Cai, E.M. Shapiro, A.D. Hamilton, Self-assembling DNA quadruplex conjugated to MRI contrast agents, Bioconjugate Chem. 20 (2009) 205–208.
[23] M. Mikawa, N. Miwa, M. Brautigam, T. Akaike, A. Maruyama, A pH-sensitive contrast agent for functional magnetic resonance imaging (MRI), Chem. Lett. 7 (1998) 693–694.
[24] M. Mikawa, N. Miwa, M. Brautigam, T. Akaike, A. Maruyama, Gd^{3+}-loaded polyion complex for pH depiction with magnetic resonance imaging, J. Biomed. Mater. Res. 49 (2000) 390–395.
[25] S.E. Plush, M. Woods, Y.-F. Zhou, S.B. Kadali, M.S. Wong, A.D. Sherry, Nanoassembled capsules as delivery vehicles for large payloads of high relaxivity Gd3+ agents, J. Am. Chem. Soc. 131 (2009) 15918–15923.
[26] P. Voisin, E.J. Ribot, S. Miraux, A.-K. Bouzier-Sore, J.-Fr. Lahitte, V. Bouchaud, S. Mornet, E. Thiaudie're, J.-M. Franconi, L. Raison, C. Labruge're, M.-H. Delville, Use of lanthanide-grafted inorganic nanoparticles as effective contrast agents for cellular uptake imaging, Bioconjugate Chem. 18 (2007) 1053–1063.

[27] Y. Matsumura, H. Maeda, A new concept for macromolecular therapeutics in cancer chemotherapy: mechanism of tumoritropic accumulation of proteins and the antitumor agent Smancs, Cancer Res. 46 (1986) 6387–6392.
[28] H.M. Aliabadi, A. Lavasanifar, Polymeric micelles for drug delivery, Expert Opin. Drug Deliv. 3 (1) (2006) 130–162.
[29] M. Yokoyama, T. Okano, Y. Sakurai, S. Fukushima, K. Okamoto, K. Kataoka, Selective delivery of adriamycin to a solid tumor using a polymeric micelle carrier system, J. Drug Target. 7 (1999) 171–186.
[30] E. Nakamura, K. Makino, T. Okano, T. Yamamoto, M. Yokoyama, A polymeric micelle MRI contrast agent with changeable relaxivity, J. Control. Release 114 (2006) 325–333.
[31] E. Kanal, D.R. Broome, D.R. Martin, H.S. Thomsen, Response to the FDA's May 23, 2007, nephrogenic systemic fibrosis update, Radiology 246 (2008) 11–14.
[32] L.M. De Leon-Rodriguez, Z. Kovacs, The synthesis and chelation chemistry of DOTA-peptide conjugates, Bioconjugate Chem. 19 (2008) 391–402.
[33] K. Shiraishi, K. Kawano, T. Minowa, Y. Maitani, M. Yokoyama, Preparation and in vivo imaging of PEG-poly(L-lysine)-based polymeric micelle MRI contrast agents, J. Control. Release 136 (2009) 14–20.
[34] A. Harada, K. Kataoka, Formation of polyion complex micelles in an aqueous milieu from a pair of oppositely-charged block copolymers with poly(ethylene glycol) segments, Macromolecules 28 (1995) 5294–5299.
[35] Y. Tajima, Biological Reference Data Book on Experimental Animals, in: Y. Tajima, S. Horiuchi (Eds.), Soft Science, Tokyo, 1989.
[36] P. Caravan, N.J. Cloutier, M.T. Greenfield, S.A. McDermid, S.U. Dunham, J.W.M. Bulte, J.C. Amedio, R.J. Looby, R.M. Supkowski, W.D. Horrocks, T.J. McMurry, R.B. Lauffer, The interaction of MS-325 with human serum albumin and its effect on proton relaxation rates, J. Am. Chem. Soc. 124 (2002) 3152–3162.
[37] S. Aime, M. Botta, S.G. Crich, G. Giovenzana, G. Palmisano, M. Sisti, Novel paramagnetic macromolecular complexes derived from the linkage of a macrocyclic Gd(III) complex to polyamino acids through a squaric acid moiety, Bioconjugate Chem. 10 (1999) 192–199.

Molecular characterization of tumors from a transgenic mouse adrenal tumor model: Comparison with human pheochromocytoma

YOSHIYUKI HATTORI[1], NAOTETSU KANAMOTO[2], KUMI KAWANO[1], HIROSHI IWAKURA[3], MASAKATSU SONE[2], MASAKO MIURA[2], AKIHIRO YASODA[2], NAOHISA TAMURA[2], HIROSHI ARAI[2], TAKASHI AKAMIZU[3], KAZUWA NAKAO[2] and YOSHIE MAITANI[1]

[1]Institute of Medicinal Chemistry, Hoshi University, Shinagawa-ku, Tokyo 142-8501; [2]Department of Medicine and Clinical Science, Kyoto University Graduate School of Medicine, Kyoto 606-8507; [3]Ghrelin Research Project, Translational Research Center, Kyoto University Hospital, Kyoto 606-8507, Japan

Received May 3, 2010; Accepted June 21, 2010

DOI: 10.3892/ijo_00000719

Abstract. Adrenal neuroblastoma and pheochromocytoma have the same embryonic origin from neural crest cells and mainly arise from the adrenal medulla. Recently, transgenic mice exhibiting tumors in the bilateral adrenal medulla by the expression of SV40 T-antigen were developed. In this study, we investigated mRNA expression in adrenal tumors of transgenic mice and compared them with human pheochromocytoma by DNA microarray analysis. To compare mouse adrenal tumors and human pheochromacytoma, we found that the expressions of noradrenergic neuron-related genes, including dopa decarboxylase, phenylethanolamine-N-methyltransferase and chromogranin B, were up-regulated in humans but not in mice; however, the expression of neuroblastoma-related genes, including Mycn, paired-like homeobox 2b, γ-aminobutyric acid A receptor ß3 subunit, islet 1 and kinesin family member 1A, was up-regulated in both species. From the gene expression profiles, the characterization of mouse adrenal tumor, may be similar to that of human adrenal neuroblastoma rather than pheochromacytomas. This mouse model would be a useful tool for the development of anti-cancer drugs and for understanding the etiology of adrenal neuroblastoma.

Introduction

Adrenal neuroblastoma and pheochromocytoma have the same embryonic origin from neural crest cells and mainly arise from the adrenal medulla. Adrenal neuroblastoma is the most common and deadly extracranial solid childhood tumor, exhibiting marked variation in clinical presentation, ranging from localized to high metastatic disease. Neuroblastoma causes 15% of cancer-related deaths in children (1). Patients with early-stage neuroblastoma, particularly those detected by a mass screening program, are known to have a good prognosis, and the tumors of these patients possess the ability to differentiate and regress spontaneously (2). In contrast, patients with advanced-stage neuroblastoma still have a poor prognosis despite recent developments in treatment (1). Pheochromocytomas are catecholamine-producing tumors that occur from chromaffin cells of adrenal medulla or extra-adrenal location, leading to paroxysmal or persistent hyper-tension in most patients (3,4). Pheochromocytoma generally occurs as a benign tumor, but 10-25% of cases are malignant at first surgery or at recurrence, with metastasis development in the lymph nodes, bone, liver or lung. Once pheochromocytoma has metastasized, there is no curative therapy; therefore, the availability of reliable tumor models for adrenal neuroblastoma and pheochromocytoma to test novel chemotherapeutic agents remains an important aspect to improve survival.

For the development of new therapeutic drugs for tumors of the adrenal medulla, *in vivo* rodent models are useful in addition to *in vitro* cultured tumor cells. In the early 1990s, adrenal medullary neoplasms were reported in transgenic mice carrying simian virus 40 (SV40) or polyoma viral T-antigens driven by a variety of promoters (5-8), including those for tyrosine hydroxylase (Th) (8) and phenylethanolamine N-methyltransferase (Pnmt) (6). Some were classified as primitive neuroectodermal tumors (9) or neuroblastoma (5). Better differentiated pheochromocytomas and hyperplastic nodules have subsequently been reported to occur with high frequency in transgenic mice expressing c-mos (10,11) or multiple endocrine neoplasia (MEN) 2B-type mutant rearranged during transfection (RET) (Met 918) (12) and in retinoblastoma (Rb) (13), phosphatase and tensin homolog deleted from chromosome (Pten) (14) or neurofibromatosis 1 (Nf1) (15) knockout mice. Unfortunately, some of these mice have not

Correspondence to: Dr Yoshiyuki Hattori, Institute of Medicinal Chemistry, Hoshi University, Shinagawa-ku, Tokyo 142-8501, Japan
E-mail: yhattori@hoshi.ac.jp

Key words: adrenal tumor, pheochromocytoma, neuroblastoma, DNA array

been maintained and may be permanently lost as experimental models.

Recently, we developed transgenic mice exhibiting tumors in the bilateral adrenal glands by the expression of SV40 T-antigen and have maintained them as a experimental model (16). Genome-wide gene expression studies will provide insight into the genes and molecular pathways that govern the pathogenesis of adrenal tumors; however, this has not been reported in adrenal tumor model mice. In this study, we investigated mRNA expression in adrenal tumors of transgenic mice and compared them with human pheochromocytoma by DNA microarray analysis.

Materials and methods

Animals. Transgenic mice carrying tetracycline inducible SV40 T-antigen, a fusion gene comprising tetracycline-responsive elements (TRE) with cytomegarovirus promoter and SV40 T-antigen were generated by microinjection of fertilized C57/B6 mouse eggs as previously reported (16). Transgenic mice were used as heterozygotes. Animal experiments were conducted with ethics approval from our institutional animal care and use committee.

Histopathology. Excised adrenal tumors from transgenic mice at the age of 5, 9, 13, 15, 17 and 21 weeks (5T, 9T, 13T, 15T, 17T and 21T, respectively) and normal adrenal gland from non-transgenic littermates at the age of 5, 9, 13 and 17 weeks (5N, 9N, 13N and 17N, respectively) were immediately frozen, sectioned 20-μm thick and mounted. The sections were stained with hematoxylin and pure eosin (H&E staining) (Muto Pure Chemicals Co., Ltd., Tokyo, Japan) for histopathological examination.

Tumor procurement. Human tumor specimens were collected from patients who underwent surgery at Kyoto University Hospital (Kyoto, Japan). Specimens were procured under Institutional Review Board-approved protocols compliant with international guidelines and with informed consent from patients. Tumor samples and normal adjacent samples were frozen and stored at -80˚C shortly after surgical resection. Total RNA was extracted from tumors using an RNeasy Midi Kit (Qiagen, Hilden, Germany). The quality and quantity of RNA were sufficient for gene expression profiling in 7 pheochromocytoma and 2 normal adjacent adrenal medulla from 2 patients with pheochromocytoma.

RT-PCR analysis. Total RNA was isolated from mouse adrenal tumors using the RNeasy Midi Kit (Qiagen). RNA yield and purity were checked by spectrometric measurements at 260 and 280 nm, and RNA electrophoresis, respectively. RT-PCR amplification was carried out as previously reported (17). The profile of PCR amplification consisted of denaturation at 94˚C for 0.5 min, primer annealing at 55˚C for 0.5 min, and elongation at 72˚C for 0.5 min for 30 cycles. For the amplification of SV40 T-antigen cDNA, the primers SV40 T-antigen-FW, 5'-AAACACTGCAGGCCAGATTT-3', and SV40 T-antigen-RW, 5'-AAATGAGCCTTGGGACTGTG-3', were used. For the amplification of mouse ß-actin cDNA, the primers ß-actin-FW, 5'-TGTGATGGTGGGAATGGGTCAG-3', and ß-actin-RW, 5'-TTTGATGTCACGCACGATTTCC-3', were used. PCR products were analyzed by 1.5% agarose gel electrophoresis in a Tris-borate-EDTA (TBE) buffer. The products were visualized by ethidium bromide staining.

Real-time RT-PCR was performed on the corresponding cDNA synthesized from each sample described above. The optimized settings were transferred to the real-time PCR protocol with the iCycler MyiQ detection system (Bio-Rad Laboratories, Hercules, CA, USA) and SYBR Green I assay (iQ™ SYBER Green Supermix, Bio-Rad Laboratories) was used for quantification. Samples were run in triplicate and the expression level of each mRNA was normalized for the amount of ß-actin in the same sample. Difference of 1 cycle was calculated as a 2-fold-change in the gene expression.

DNA microarray. For DNA microarray experiments, 0.5 μg aliquots of total RNA from 13N, 13T, 15T, 17T and human tumor specimens were labeled using the Quick Amp Labeling Kit (Agilent Technologies, Santa Clara, CA, USA) according to the manufacturer's instructions. After purification of Cy3-labeled cRNA with RNeasy mini spin columns (Qiagen), 1.65 μg aliquots of Cy3-labeled cRNA were hybridized to Whole Mouse genome Oligo Microarray 44K x 4 (Agilent Technologies) or Whole Human genome Oligo Microarray 44K x 4 (Agilent Technologies) using the manufacturer's hybridization protocol. After the washing step, the microarray slides were analyzed with an Agilent Technologies Microarray scanner.

For further analysis, the data were imported into the GeneSpring® 10 Software (Agilent Technologies) and normalized by median centering of arrays and genes. In mouse adrenal tumors, all transcripts showed a minimum change in the expression level of at least 10-fold compared with the adrenal gland of normal mice. In a comparison of the expression profiles between mouse and human adrenal tumors, hierarchical clustering of the above identified genes in mouse adrenal tumor and image plots using available human orthologues in pheochromocytoma were displayed with gene ordering based on hierarchical clustering of the mouse data set.

Results

Tumor appearance and SV40 T-antigen expression. We previously reported that the ectopic expression of SV40 T-antigen in adrenal medulla developed bilateral adrenal tumors at 12-13 weeks of age in mice (16). In hematoxylin and eosin-stained sections of adrenal glands, mild hyperplasia in the adrenal medulla of transgenic mice was already observed at 5 and 9 weeks of age (Fig. 1A, B, E and F). Subsequently, transgenic mice, beginning at 13 weeks of the age, developed carcinoma of the adrenal gland (Figs. 1I, J and 2A), and by 15 weeks of age, most adrenal tumors were between 0.5 and 1.0 cm in diameter (Fig. 2A). At 17 weeks of the age, tumors of the adrenal glands had enlarged to 1.0-1.5 cm diameter, and at 21 weeks of age, to 1.5-2.0 cm. The tumors in 17T were composed of undifferentiated cells with a large nucleus (Fig. 1M and N) compared with adrenal glands in non-transgenic mice.

Next, we confirmed the expression levels of SV40 T-antigen mRNA in the developing tumors of transgenic mice.

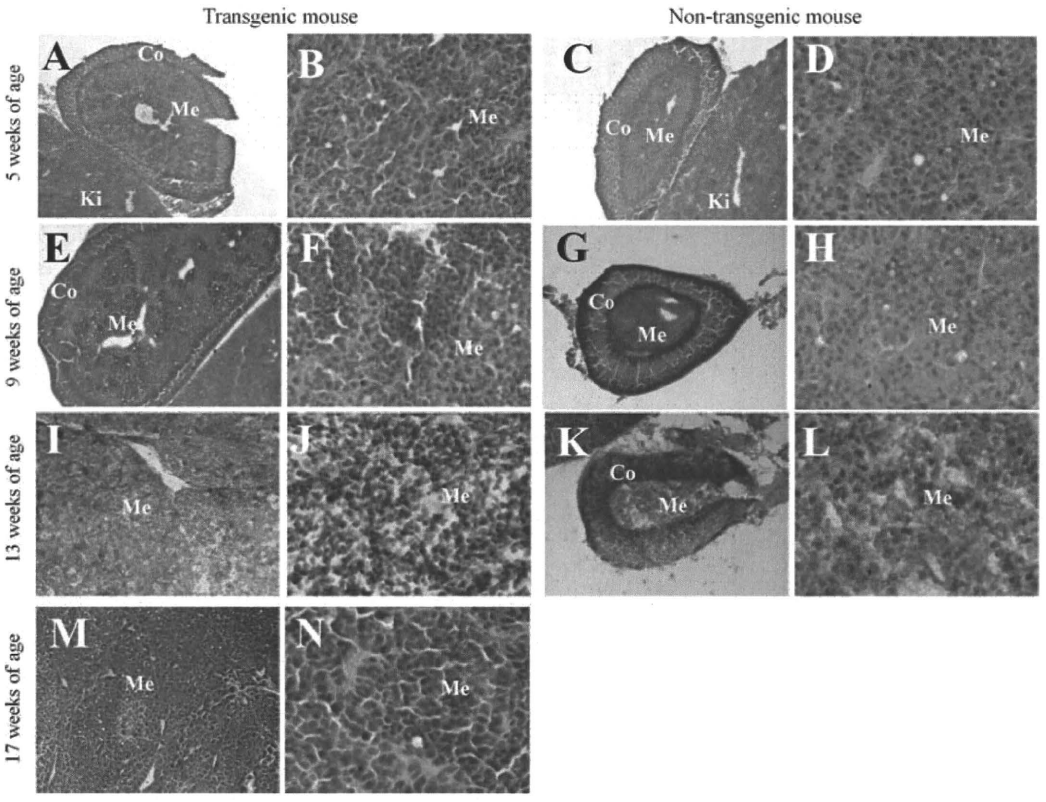

Figure 1. Histological analysis of adrenal gland from transgenic mouse. Histological section of adrenal gland from transgenic mice (A, B, E, F, I, J, M and N) and non-transgenic (C, D, G, H, K and L) mice at 5 weeks (A-D), 9 weeks (E-H), 13 weeks (I-L) and 17 weeks of age (M and N). In B, D, F, H, J, L and N, adrenal medulla in A, C, E, G, I, K and M were enlarged, respectively. H&E staining, x40 in A, C, E, G, I, K and M, x100 in B, D, F, H, J, L and N. Co, cortex of adrenal gland; Me, medulla of adrenal gland; Ki, kidney.

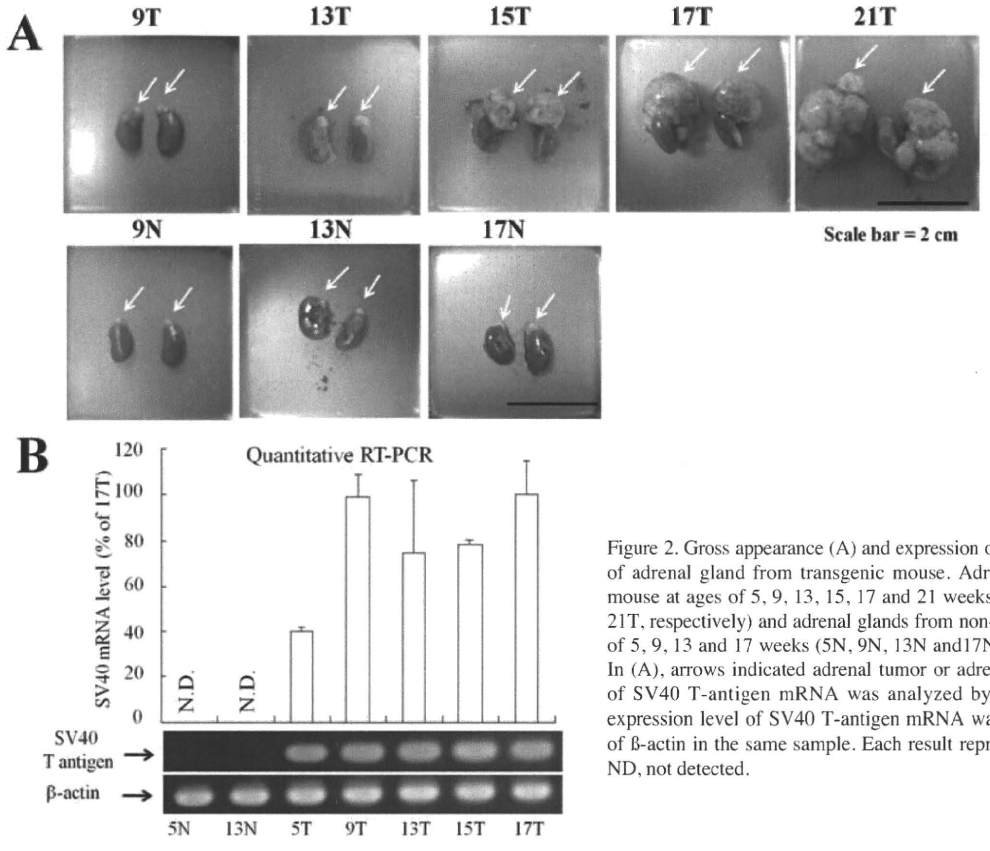

Figure 2. Gross appearance (A) and expression of SV40 T-antigen mRNA (B) of adrenal gland from transgenic mouse. Adrenal tumors from transgenic mouse at ages of 5, 9, 13, 15, 17 and 21 weeks (5T, 9T, 13T, 15T, 17T and 21T, respectively) and adrenal glands from non-transgenic littermates at ages of 5, 9, 13 and 17 weeks (5N, 9N, 13N and17N, respectively) were excised. In (A), arrows indicated adrenal tumor or adrenal gland. In (B), expression of SV40 T-antigen mRNA was analyzed by quantitative RT-PCR. The expression level of SV40 T-antigen mRNA was normalized for the amount of ß-actin in the same sample. Each result represents the mean ± SD (n=3). ND, not detected.

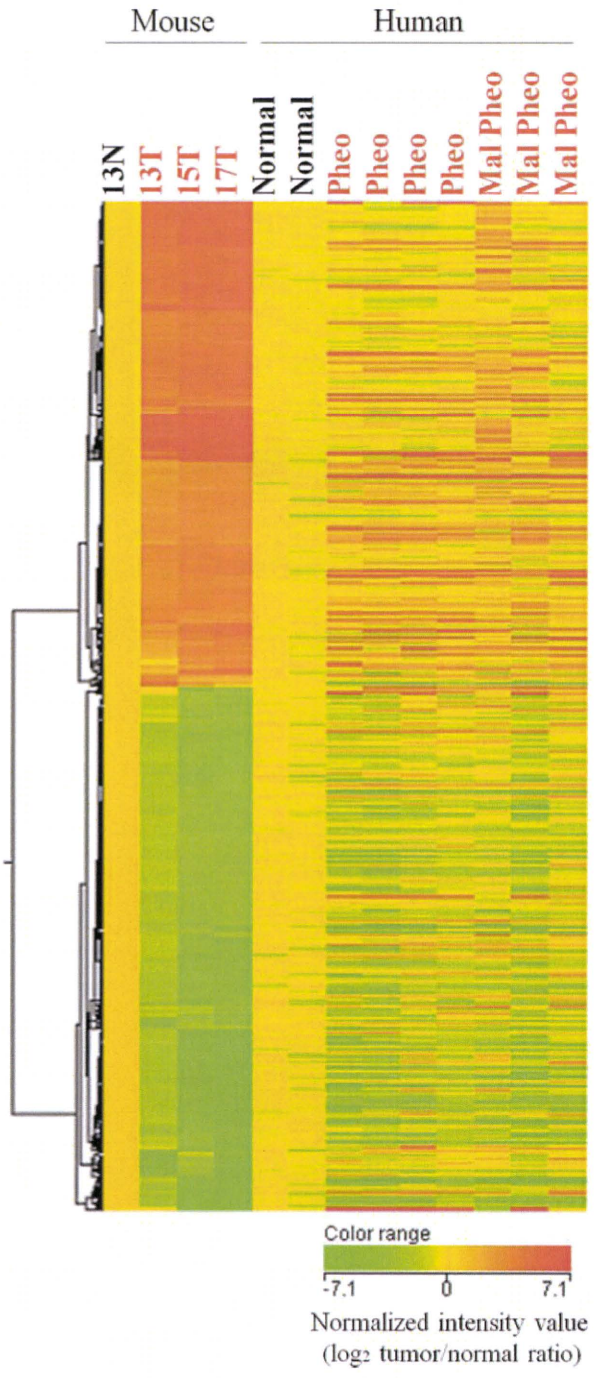

Figure 3. Gene expression patterns of mouse adrenal tumor-specific signature in human pheochromocytoma. Hierarchical clustering of mouse adrenal tumors (13T, 15T and 17T)-specific genes (~2,500 genes), which were >10-fold higher and lower than in the normal adrenal gland (13N), and image plots using available human orthologues in pheochromocytoma are shown with gene ordering based on hierarchical clustering of the mouse data set. Expression profiles in four benign pheochromocytomas (Pheo), three malignant pheochromocytomas (Mal Pheo) and two normal adjacent adrenal medulla (normal) were aligned beside those in mouse tumors. Genes with a relatively higher level of expression are shown in red and those with a lower level of expression in green.

Expression levels of SV40 T-antigen from 5T to 17T were similar, but those in 5N and 13N were not detected (Fig. 2B), suggesting that SV40 T-antigen was expressed in adrenal glands of transgenic mice at an early age and induced adrenal hyperplasia.

Comparison of gene expression patterns between mouse adrenal tumor and human pheochromocytoma. Cells of adrenal neuroblastomas have neuroblastic morphology and do not express the adrenal chromaffin marker Pmnt, but they share phenotypic characteristics with immature sympathetic neuroblasts present as nests of cells in the developing adrenal gland (18). Although sympathetic neurons and chromaffin cells are developmentally related and functionally similar, a defining functional difference between the two cell types is that only chromaffin cells express Pmnt (18).

We compared the expression profile of transgenic mice with that of human pheochromocytoma by DNA microarray (Fig. 3). To investigate mRNA expression in developing adrenal tumors of transgenic mice, we used RNA of adrenal tumors from 13T, 15T and 17T, and of the normal adrenal gland from 13N as a control. Overall, the expression patterns of up- and down-regulated genes in both human benign and malignant pheochromocytomas were similar with those in mouse adrenal tumors (Fig. 3). Furthermore, the expression profile in benign pheochromocytomas was very similar to that in malignant pheochromocytomas, therefore, in subsequent analysis, we used average of four benign and three malignant pheochromocytomas for comparison of expression level with mouse adrenal tumors. In adrenal tumors of transgenic mice, Pmnt expression was absent and other noradrenergic synthesis-related genes also greatly reduced compared with in normal adrenal gland, although up-regulated in human pheochromacytoma (Table I). It has been reported that Pmnt expression was absent or greatly reduced in tumors associated with viral T-antigens (8,19). Furthermore, no difference in blood pressure between transgenic and non-transgenic mice was observed (~60 mmHg in mean blood pressure) (data not shown). These findings indicated that the characteristics of human pheochromocytoma regarding noradrenergic secretion and hypertension were dissimilar to those of mouse adrenal tumors.

Recently, Cheung *et al* have reported that cyclin D1 (CCND1), dopa decarboxylase (DDC), γ-aminobutyric acid A receptor ß3 subunit (GABRB3), islet 1 (ISL1), kinesin family member 1A (KIF1A), and paired-like homeobox 2b (PHOX2B) were abundantly expressed in stage IV human neuroblastoma tumors and these expressions were useful in predicting patient outcome (20). In both mouse and human adrenal tumors, Phox2b, Gabrb3, Isl1 and Kif1a were also up-regulated (Table I). Furthermore, we found 49 up-regulated genes and 66 down-regulated genes which were >10-fold different between a normal adrenal gland and the adrenal tumor in both mice and humans (Tables II and III). Among them, we found that the expressions of doublecortin and CaM kinase-like 1 (Dclk1), dihydropyrimidinase-like 3 (Dpysl3), embryonic lethal, abnormal vision, Drosophila-like 3 (Elavl3), GATA binding protein 2 (Gata2), GATA binding protein 3 (Gata3), hairy/enhancer-of-split related with YRPW motif 1 (Hay1), myelin transcription factor 1-like (Myt1l), transgelin 3 (Tagln3), and transcription factor AP-2 ß (Tcfap2b), which are related to nervous system development, were strongly up-regulated in both human and mouse adrenal tumors (Table II), and the expression of many genes related to lipid metabolic

Table I. Adrenal gland-related genes in human pheochromocytoma and mouse adrenal tumors as shown by cDNA microarray.

Gene symbol	Description	Gene expression (log_2 tumor/normal ratio)				Biological process
		13T/13N	15T/13N	17T/13N	Pheo/ normal	
Noradrenergic neuron-related genes						
Ddc	Dopa decarboxylase	0.64	-3.11	-1.14	7.91	Catecholamine biosynthetic process
Th	Tyrosine hydroxylase	1.06	0.16	-0.30	7.91	Dopamine biosynthetic process from tyrosine
Dbh	Dopamine ß hydroxylase	1.20	1.33	0.89	7.33	Catecholamine metabolic process
Pnmt	Phenylethanolamine-N-methyltransferase	-0.08	-6.33	-8.53	6.10	Catecholamine biosynthetic process
Chga	Chromogranin A	0.17	0.09	-0.18	7.80	
Chgb	Chromogranin B	-0.24	-0.21	-0.06	5.96	
Npy	Neuropeptide Y	-0.08	-0.50	-0.70	7.39	Neuropeptide signaling pathway
Slc6a2	Solute carrier family 6, member 2	2.47	1.25	0.28	7.99	Neurotransmitter transport
Neuroblastoma-related genes						
Phox2b	Paired-like homeobox 2b	1.49	1.86	1.94	9.04	Regulation of transcription
Mycn	V-myc myelocytomatosis viral related oncogene, neuroblastoma derived	0.76	0.97	1.47	5.79	Regulation of progression through cell cycle
Ccnd1	Cyclin D1	-1.97	-3.11	-3.42	0.67	Regulation of progression through cell cycle
Crmp1	Collapsin response mediator protein 1	2.74	3.34	3.27	6.19	
Gabrb3	γ-aminobutyric acid receptor, subunit ß3	2.98	2.82	2.64	4.45	γ-aminobutyric acid signaling pathway
Isl1	ISL1 transcription factor, LIM/homeodomain	4.24	5.99	6.17	4.36	Regulation of transcription
Kif1a	Kinesin family member 1A	0.48	1.50	1.61	6.17	Microtubule-based process

Pheo, human pheochromocytoma; normal, human normal adrenal medulla.

process and electron transport was strongly down-regulated (Table III). The reasons for suppression of the metabolism might be that energy (ATP) in tumor cells is mainly or only provided by glycolysis in the cytoplasm and suppresses oxidative phosphorylation in mitochondria (Warburg effect) (21).

We also found that G protein-regulated inducer of neurite outgrowth 1 (Grin1) (22), insulin-like growth factor 2 gene (Igf2) (23), embryonic lethal, abnormal vision, Drosophila-like 4 (Elavl4) (24), and cadherin-like 22 (Cdh22) (25), which are known to relate with neuroblastoma progression, were strongly up-regulated in both mouse and human adrenal tumors (Table II). These identified genes might be important for the development of adrenal tumors in mice and humans. From gene expression profiles, the characterization of mouse adrenal tumor might be similar to that of human adrenal neuroblastoma rather than pheochromacytoma.

Discussion

In this study, we investigated mRNA expression in adrenal tumors of transgenic mice carrying SV40 T-antigen by DNA microarray analysis. The SV40 T-antigen oncoprotein binds to and functionally inactivates two major tumor suppressor genes, Rb and p53, which are often involved in many human tumors, and strongly affects many genes associated with DNA replication, damage repair, cytokinesis, and chromosome maintenance. It has been reported that proliferative gene expression patterns driven by the SV40 T-antigen were shared by transgenic mice carrying SV40 T-antigen, which

Table II. The highly up-regulated (>10-fold) genes both in human pheochromocytoma and mouse adrenal tumor (17T) as shown by cDNA microarray.

Gene symbol	Description	Gene expression (log_2 tumor/normal ratio)				Biological process
		13T/13N	15T/13N	17T/13N	Pheo/ normal	
A2bp1	Ataxin 2-binding protein 1	3.02	3.72	3.45	3.45	
Abcc8	ATP-binding cassette, sub-family C, member 8	3.54	4.94	4.93	4.64	Carbohydrate metabolic process
Bai3	Brain-specific angiogenesis inhibitor 3	4.23	5.11	5.17	4.23	Signal transduction
Cartpt	CART prepropeptide	6.52	6.56	5.83	6.21	Neuropeptide signaling pathway
Cdh22	Cadherin-like 22	3.06	3.72	3.52	7.70	Cell adhesion
Celsr3	Cadherin, EGF LAG seven-pass G-type receptor 3	3.31	3.54	3.54	5.74	Neuropeptide signaling pathway
Chrm2	Cholinergic receptor, muscarinic 2	-0.29	2.94	3.38	3.45	Signal transduction
Chrna5	Cholinergic receptor, nicotinic, α5	3.55	3.65	3.96	3.46	Signal transduction
Clgn	Calmegin	5.16	6.18	6.40	7.56	Protein folding
Coro2a	Coronin, actin binding protein, 2A	3.22	3.65	3.43	3.95	
Crtac1	Cartilage acidic protein 1	5.25	6.00	5.99	3.79	
Cryba2	Crystallin, ßA2	4.42	4.53	5.02	7.99	
Dclk1	Doublecortin and CaM kinase-like 1	4.57	6.38	6.83	5.93	Nervous system development
Dpysl3	Dihydropyrimidinase-like 3	2.66	4.26	4.64	3.90	Nervous system development
Elavl3	ELAV-like 3	4.48	5.20	5.31	4.01	Nervous system development
Elavl4	ELAV-like 4	5.01	6.07	5.90	6.22	mRNA processing
Elavl4	Elongation of very long chain fatty acids-like 4	5.64	6.05	5.85	3.87	Fatty acid biosynthetic process
Erc2	ELKS/RAB6-interacting/ CAST family member 2	4.07	3.75	3.90	3.89	Synaptogenesis
Flrt1	Fibronectin leucine rich transmembrane protein 1	3.46	3.22	3.56	5.53	
Galnt6	UDP-N-acetyl-α-D-galactosamine: polypeptide N-acetylgalactosaminyl transferase 6	4.21	4.75	4.23	3.78	Protein amino acid O-linked glycosylation
Gata2	GATA binding protein 2	4.27	3.91	4.02	5.50	Neuron differentiation
Gata3	GATA binding protein 3	3.46	3.89	3.87	4.87	Nervous system development
Gpr68	G protein-coupled receptor 68	4.02	4.98	4.53	4.07	Signal transduction
Gprin1	G protein regulated inducer of neurite outgrowth 1	3.43	3.98	3.83	4.38	
Hand1	Heart and neural crest derivatives expressed 1	5.04	4.99	4.70	4.36	Angiogenesis
Hey1	Hairy/enhancer-of-split related with YRPW motif 1	3.43	3.84	4.21	4.79	Nervous system development
Igf2	Insulin-like growth factor 2	3.87	2.60	3.34	3.55	Cell proliferation
Isl1	ISL1 transcription factor, LIM/homeodomain	4.24	5.99	6.17	4.36	Multicellular organismal development

Table II. Continued.

Gene symbol	Description	Gene expression (log_2 tumor/normal ratio)				Biological process
		13T/13N	15T/13N	17T/13N	Pheo/ normal	
Kcnj12	Potassium inwardly-rectifying channel, sub-family J, member 12	3.10	3.86	3.77	3.46	Ion transport
Kif5a	Kinesin family member 5A	3.74	4.45	4.63	3.58	Microtubule-based movement
Kl	Klotho	1.29	3.56	3.75	5.34	Metabolic process
Lingo1	Eucine rich repeat and Ig domain containing 1	6.47	6.63	6.53	4.59	
Lmo1	LIM domain only 1	3.06	4.47	4.23	5.33	Cell proliferation
Mab21l1	Mab-21-like 1	4.67	5.23	5.05	5.14	Anatomical structure morphogenesis
Mgat5b	Mannosyl (α1,6)-glycoprotein ß-1,6-N-acetyl -glucosaminyltransferase	2.49	3.04	3.64	3.53	
Myt1l	Myelin transcription factor 1-like	3.46	3.31	3.41	3.60	Nervous system development
Nefl	Neurofilament, light polypeptide 68 kDa	4.53	6.79	6.94	8.23	
Prph1	Peripherin	4.82	6.05	6.33	7.53	
Rab39b	RAB39B, member RAS oncogene family	3.76	4.52	4.11	4.70	Protein transport
Rimbp2	RIMS binding protein 2	3.65	4.72	4.46	5.66	
Slc10a4	Solute carrier family 10, member 4	2.46	4.01	4.01	6.92	Ion transport
Stac	SH3 and cysteine rich domain	2.13	3.66	3.60	3.74	Intracellular signaling cascade
Stmn4	Stathmin-like 4	5.06	6.03	5.50	5.86	Intracellular signaling cascade
Syt11	Synaptotagmin XI	3.66	4.13	4.25	4.59	Transport
Tagln3	Transgelin 3	2.84	3.74	3.72	7.25	Nervous system development
Tcfap2b	Transcription factor AP-2 ß protein 2	5.06	5.08	5.19	7.75	Nervous system development
Thbs4	Thrombospondin 4	3.36	6.29	6.19	4.07	Cell adhesion
Tm6sf2	Transmembrane 6 superfamily member 2	-0.10	0.93	4.49	3.48	
Tmem145	Transmembrane protein 145	3.19	3.14	3.39	4.25	
Tubb2b	Tubulin, ß 2B	3.35	5.00	4.84	6.90	Microtubule-based movement

Pheo, human pheochromocytoma; normal, human normal adrenal medulla.

developed breast tumor (C3(1)/Tag transgenic mice driven by rat prostate steroid binding protein promoter), lung tumor (CC10-Tag transgenic mice driven by mouse clara cell secretory protein promoter), and prostate tumor (TRAMP transgenic mouse driven by rat probasin promoter) (26). Therefore, we compared the expression profiles of the SV40 T-antigen signature between adrenal tumors and three tumor types of transgenic mice carrying SV40 T-antigen, and the expression profile of mouse adrenal tumor was very similar to other tumor types of transgenic mouse (data not shown).

The SV40 T-antigen gene signature was not a feature of tumors initiated by other oncogenes or inactivation of suppressor genes but is most specific to tumors induced by T-antigen (26). Transgenic overexpression of myc, ras, HER-2/neu, and polyoma viral middle T-antigen (PyMT) oncogenes driven by mouse mammary tumor virus (MMTV) promoter were most dissimilar to those of SV40 T-antigen in gene expression profiles; however, SV40 T-antigen viral oncoprotein can cause an intrinsic gene expression profile that recapitulates the aggressive phenotypes of aggressive

Table III. The highly down-regulated (>10-fold) genes both in human pheochromocytoma and mouse adrenal tumor (17T) as shown by cDNA microarray.

Gene symbol	Description	Gene expression (log_2 tumor/normal ratio)				Biological process
		13T/13N	15T/13N	17T/13N	Pheo/ normal	
Aadac	Arylacetamide deacetylase	-6.00	-3.34	-6.80	-9.25	Metabolic process
Abca8b	ATP-binding cassette, sub-family A, member 8	-1.29	-2.50	-3.94	-3.71	Transport
Abcb1a	ATP-binding cassette, sub-family B, member 1	-2.15	-4.34	-3.98	-3.56	Transport
Abcb4	Homo sapiens ATP-binding cassette, sub-family B, member 4	-2.60	-5.65	-5.95	-3.95	Lipid metabolic process
Ace2	Angiotensin I converting enzyme 2	-1.63	-3.13	-5.97	-4.09	Proteolysis
Adh1	Alcohol dehydrogenase 1C, γ polypeptide	-1.87	-5.69	-7.09	-3.68	Alcohol metabolic process
Adh4	Alcohol dehydrogenase 4, pi polypeptide	-4.96	-2.80	-4.09	-4.33	Alcohol metabolic process
Agtr1a	Angiotensin II receptor, type 1	-2.00	-5.16	-5.90	-3.53	Signal transduction
Alas1	Aminolevulinate, Δ, synthase 1	-2.40	-5.64	-5.98	-4.69	Biosynthetic process
Aldh1l1	Aldehyde dehydrogenase 1 family, member L1	-2.60	-5.11	-5.71	-5.24	Biosynthetic process
Aldob	Aldolase B, fructose-bisphosphate	-5.84	-2.99	-6.61	-3.87	Metabolic process
Aox1	Aldehyde oxidase 1	-2.47	-5.25	-5.28	-7.73	Electron transport
Apoc1	Apolipoprotein C-I	-3.17	-3.52	-5.65	-6.02	Lipid metabolic process
Baiap2l1	BAI1-associated protein 2-like 1	-2.25	-3.82	-3.40	-3.74	
C3	Complement component 3	-3.32	-5.79	-7.26	-3.63	Signal transduction
C4b	Complement component 4B	-2.39	-3.31	-4.23	-5.20	Inflammatory response
Ccbe1	Collagen and calcium binding EGF domains 1	-2.52	-7.10	-8.16	-4.00	Phosphate transport
Cfi	Complement factor I	-5.94	-2.31	-4.75	-4.28	Proteolysis
Cldn1	Claudin 1	-2.01	-4.58	-3.63	-4.55	Cell adhesion
Cp	Ceruloplasmin	-2.31	-3.24	-3.89	-4.40	Ion transport
Cpb1	Carboxypeptidase B1	-2.45	-8.04	-8.28	-7.08	Proteolysis
Cth	Cystathionase	-2.70	-4.11	-4.63	-4.16	Amino acid biosynthetic process
Cyp11a1	Cytochrome P450, family 11 subfamily A, polypeptide 1	-2.37	-6.60	-8.45	-7.31	Lipid metabolic process
Cyp11b2	Cytochrome P450, family 11, subfamily B, polypeptide 2	-2.60	-8.00	-8.52	-10.92	Lipid metabolic process
Cyp21a1	Cytochrome P450, family 21, subfamily A, polypeptide 2	-2.94	-7.98	-8.85	-9.26	Electron transport
Dab2	Disabled homolog 2, mitogen-responsive phosphoprotein	-2.09	-4.78	-4.81	-3.50	Cell proliferation
Ephx1	Epoxide hydrolase 1, microsomal	-2.11	-3.39	-3.50	-5.78	Xenobiotic metabolic process

Table III. Continued.

Gene symbol	Description	Gene expression (log_2 tumor/normal ratio) 13T/13N	15T/13N	17T/13N	Pheo/normal	Biological process
Fbp1	Fructose-1,6-bisphosphatase 1	-4.55	-3.04	-5.59	-3.58	Carbohydrate metabolic process
Fdx1	Ferredoxin 1,	-1.68	-4.92	-5.41	-5.51	Steroid metabolic process
Fdxr	Ferredoxin reductase	-2.63	-5.59	-5.71	-5.11	Lipid metabolic process
Fgg	Fibrinogen γ chain, transcript variant γA	-5.63	-1.67	-4.92	-3.83	Signal transduction
Fmo2	Flavin containing monooxygenase 2 (non-functional)	-2.09	-4.05	-4.94	-3.48	Electron transport
Fmo3	Flavin containing monooxygenase 3	-4.03	-6.19	-5.74	-3.60	Electron transport
Galm	Galactose mutarotase	-2.84	-3.59	-3.76	-4.61	Carbohydrate metabolic process
Gata6	GATA binding protein 6	-2.36	-4.96	-5.60	-5.41	Positive regulation of transcription
Gckr	Glucokinase regulator	-4.45	-2.80	-3.94	-3.75	Cell glucose homeostasis
Gja1	Gap junction protein, α1, 43 kDa	-2.20	-4.26	-4.26	-4.24	Transport
Gsta3	Glutathione S-transferase A3	-2.30	-4.07	-6.29	-9.05	Metabolic process
Hsd11b1	Hydroxysteroid (11ß) dehydrogenase 1	-2.18	-3.53	-4.40	-3.95	Metabolic process
Hsd3b1	Hydroxy-Δ-5-steroid dehydrogenase, 3ß- and steroid Δ-isomerase 1	-2.70	-6.67	-8.14	-11.81	Steroid biosynthetic process
Inmt	Indolethylamine N-methyltransferase	-3.51	-3.56	-5.86	-3.36	
Kcnk3	Potassium channel, subfamily K, member 3	-2.40	-4.59	-5.16	-3.46	Ion transport
Kcnn2	Potassium intermediate/small conductance calcium-activated channel, subfamily N, member 2	-1.87	-6.01	-7.75	-4.25	Ion transport
Ly6d	Lymphocyte antigen 6 complex, locus D	-2.35	-7.54	-9.04	-5.49	Cell adhesion
Mc2r	Melanocortin 2 receptor	-2.54	-6.00	-6.44	-5.29	Signal transduction
Mgst1	Microsomal glutathione S-transferase 1	-2.11	-5.55	-6.29	-7.98	Glutathione metabolic process
Mlxipl	MLX interacting protein-like	-1.75	-4.33	-5.82	-5.18	Regulation of transcription
Mrap	Melanocortin 2 receptor accessory protein	-2.60	-7.07	-8.40	-6.05	
Nr0b1	Nuclear receptor subfamily 0, group B, member 1	-2.63	-7.14	-8.16	-9.23	Adrenal gland development
Nr0b2	Nuclear receptor subfamily 0, group B, member 2	-2.89	-4.98	-5.17	-6.43	Cholesterol metabolic process
Nr1h4	Nuclear receptor subfamily 1, group H, member 4	-2.74	-4.58	-6.70	-6.93	Transcription
Nr5a1	Nuclear receptor subfamily 5, group A, member 1	-2.24	-4.95	-5.14	-5.45	Transcription

Table III. Continued.

Gene symbol	Description	Gene expression (log_2 tumor/normal ratio)				Biological process
		13T/13N	15T/13N	17T/13N	Pheo/ normal	
Pdgfra	Platelet-derived growth factor receptor α polypeptide	-2.13	-3.83	-4.69	-4.61	Cell proliferation
Prlr	Prolactin receptor	-2.36	-4.45	-4.63	-3.46	Steroid biosynthetic process
Rgn	Regucalcin	-4.31	-3.35	-6.08	-5.15	
Rnf43	Ring finger protein 43	-2.58	-4.67	-6.19	-4.94	
Scarb1	Scavenger receptor class B, member 1	-2.13	-5.29	-5.83	-5.53	Cholesterol metabolic process
Sec14l4	SEC14-like 4	-2.44	-3.45	-6.50	-3.53	Transport
Slc37a2	Solute carrier family 37, member 2	-2.19	-3.17	-3.77	-4.60	Transport
Soat1	Sterol O-acyltransferase 1	-2.72	-4.95	-5.38	-4.39	Lipid metabolic process
Star	Steroidogenic acute regulator, nuclear gene encoding mitochondrial protein	-1.73	-6.67	-8.63	-8.64	Steroid biosynthetic process
Steap4	STEAP family member 4	-1.68	-2.51	-3.96	-3.50	Electron transport
Tbx3	T-box 3	-1.86	-4.69	-5.22	-4.77	Anti-apoptosis
Tcf21	Transcription factor 21	-2.07	-2.76	-5.20	-3.88	Organ morphogenesis
Tspan12	Tetraspanin 12	-2.09	-4.89	-5.29	-3.49	
Tst	Thiosulfate sulfurtransferase	-2.44	-4.79	-5.00	-4.70	Sulfate transport
Wnt4	Wingless-type MMTV integration site family, member 4	-2.86	-7.27	-7.73	-3.78	Multicellular organismal development

Pheo, human pheochromocytoma; normal, human normal adrenal medulla.

human cancers (26). In hematoxylin and eosin-stained sections, mouse adrenal tumor was composed of undifferentiated cells with a large nucleus (Fig. 1M and N). From comparison of the gene expression profiles by hierarchical clustering, up- or down-regulated genes in mouse adrenal tumor were overall similar to those in human pheochromocytoma (Fig. 3), but the expression patterns of noradrenergic neuron-related genes in mouse adrenal tumor were dissimilar with those in human pheochromocytoma (Table I), indicating that the characterization of mouse adrenal tumor was similar to that of human adrenal neuroblastoma rather than pheochromocytoma. This transgenic mouse might be a useful model of undifferentiated and aggressive adrenal neuroblastoma.

Researchers are studying chemotherapy drugs in order to find an effective therapy for neuroblastoma. In chemotherapy for high-risk neuroblastoma, the following drugs are often used: cyclophosphamide, ifosfamide, cisplatin, carboplatin, vincristine, doxorubicin (DXR), melphalan, etoposide (VP-16), teniposide (VM-26), and topotecan. In this study, we found that the expression of DNA topoisomerase II (Topo IIα) mRNA in adrenal tumors of transgenic mice increased 120-150-fold compared to non-transgenic mice (data not shown); therefore, we investigated the antitumor effect for transgenic mice by DXR, which is an inhibitor of Topo IIα. As a result, i.v. administration of DXR could suppress tumor growth significantly (data not shown), corresponding with the prognostic results from DNA array; therefore, this mouse model would be a useful tool for the development of anti-cancer drugs of neuroblastoma.

Acknowledgements

This study was supported in part by a Grant-in-Aid for Scientific Research from the Ministry of Education, Culture, Sports, Science, and Technology of Japan, and by the Open Research Center Project.

References

1. Brodeur GM, Maris JM, Yamashiro DJ, Hogarty MD and White PS: Biology and genetics of human neuroblastomas. J Pediatr Hematol Oncol 19: 93-101, 1997.
2. Yamamoto K, Hanada R, Kikuchi A, *et al*: Spontaneous regression of localized neuroblastoma detected by mass screening. J Clin Oncol 16: 1265-1269, 1998.
3. Tischler AS: Pheochromocytoma and extra-adrenal paraganglioma: updates. Arch Pathol Lab Med 132: 1272-1284, 2008.
4. Adler JT, Meyer-Rochow GY, Chen H, *et al*: Pheochromocytoma: current approaches and future directions. Oncologist 13: 779-793, 2008.